Reproduction Experiments of Radial Pyroxene Chondrules using Gas-jet Levitation System under Reduced Condition

Kana Watanabe*, Tomoki Nakamura, and Tomoyo Morita

Department of Earth Science, Tohoku University, Sendai

980-8578, Japan.

Abstract

Reproduction experiments of radial pyroxene (RP) chondrules were carried out using Ar-H_2 or Ar gas-jet levitation system in a reduced atmosphere in order to simulate chondrule formation in the protoplanetary disk. The experiments reproduced RP-chondrule texture, consisting of sets of thin pyroxene crystals and mesostasis glass between crystals. However, iron partition coefficients between pyroxene and glassy mesostasis in natural RP chondrules (D_{Fe} = Fe mol%$_{pyroxene}$/Fe mol%$_{mesostasis}$) were much higher than that in experimentally reproduced RP chondrules. The high D_{Fe} in natural RP chondrules suggest that iron was removed from the mesostasis melt at high temperatures after the crystal growth of pyroxene. We found that many small iron-metal inclusions had formed in the mesostasis glass, indicating that FeO in the high-temperature melt of mesostasis was reduced to metallic iron, and iron in the mesostasis was diffused into newly-formed metal inclusions. The formation of the iron-metal inclusions in the mesostasis was reproduced by our experiments in a reduced atmosphere, confirming that D_{Fe} in natural RP chondrules increased after the crystal growth of radial pyroxenes. Therefore, D_{Fe} of RP chondrules can be an indicator to constrain cooling rates and redox states during the chondrule formation.

* Corresponding author: Kana Watanabe
 kana.watanabe.t3@alumni.tohoku.ac.jp

1. Introduction

Chondrules are silicate spherules with diameters varying from several tens of micrometers to several millimeters and are the main components of chondrites. They formed by melting precursor dust particles at high temperatures and subsequent crystallization during cooling in the protoplanetary disk within 5 Myr after the formation of calcium–aluminum-rich inclusions (CAIs) (e.g., Kita & Ushikubo 2012; Bollard et al. 2015; Pape et al. 2019). Various formation models have been proposed, such as lightning models (Whipple 1966; Desch & Cuzzi 2000; Johansen & Okuzumi 2018), shock wave models (Connolly & Love 1998b; Ciesla & Hood 2002; Morris & Desch 2010), and planetesimal collision models (Kieffer 1975; Johnson et al. 2014, 2015; Wakita et al. 2017), but no widely-accepted, definitive model exists at present. Constraints of the chondrule formation process lead to understanding the temperature profiles and gas compositions of the protoplanetary disk.

Reproduction experiments of chondrules have been carried out to understand the chondrule formation process. They revealed that morphological characteristics of crystals are resulted from peak temperatures and cooling rates during chondrule crystallization (Tsuchiyama et al. 1980; Tsuchiyama and Nagahara 1981; Hewins 1983; Lofgren & Russell 1986; Lofgren 1989; Hewins & Radomsky 1990; Lofgren & Lanier 1990; Connolly et al. 1998). However, in most of these experiments, starting materials are fixed to Pt or Pt-Rh wires. The wire method is unsuitable for discussing the crystallization process in the protoplanetary disk because contact points between starting materials and wires work as heterogeneous nucleation sites and facilitate crystallization. For this reason, levitation experiments have been conducted to simulate chondrule formation (Tsukamoto et al. 1999; Nagashima et al. 2006, 2008; Pack et al. 2010; Mishra et al. 2020).

However, levitation experiments that simulate the redox state of the chondrule-forming regions and the natural chondrule compositions are insufficient. The chondrule formation took place under reduced conditions (e.g., Grossman et al. 2008; Villeneuve et al. 2015), and the natural chondrules contain multiple elements as major and minor elements. Especially, iron is

the crucial element responsible for chondrule compositional variations, such as type-I and -II chondrules (McSween 1977; Scott & Taylor 1983). Mishra et al. (2020) and Shete et al. (2021) conducted the levitation experiments under low pressure or Ar gas apparatuses that simulate the atmosphere of chondrule formation, but the starting materials were pure forsterite or enstatite. Pack et al. (2010) concentrated on the evaporation of alkalis and confirmed the metal formation of chondrules under Ar or Ar-H_2 atmosphere. The crystal morphologies and elemental behaviors in experiments conducted under reduced conditions using natural chondrule compositions remain to be understood.

In this study, we conducted reproduction experiments of radial pyroxene (RP) chondrules by the gas-levitation system in a closed container under reduced conditions (ΔIW-1.8 to ΔIW+1.9, ΔIW (iron-wustite) $\equiv \log(fO_2) - \log(fO_2)_{IW}$), which were close to the oxygen fugacities in the protoplanetary disk. The starting materials had natural RP compositions, including iron. It is known that RP chondrules crystallized from totally melted precursor materials (Connolly & Hewins 1995) through heterogeneous nucleation by dust collisions (Nagashima et al. 2006). The levitation experiment is suitable for the reproduction of RP chondrules because our experimental procedure can simulate dust collisions with a floating melt sphere. In order to reproduce the heterogeneous nucleation of RP chondrules, in this study, a small amount of powder of starting materials collided with a chondrule melt sphere of supercooling as seeds to promote heterogeneous nucleation. This simulates the collisions with interplanetary dust during chondrule formation in the protoplanetary disk. In the reduced condition and with the procedure of particle collision, we performed the experiments by melting starting materials containing iron. We compared the crystal morphologies and chemical compositions of natural RP chondrules with those of experimentally reproduced chondrules.

2. METHODS

2.1. Reproduction Experiments of RP Chondrules

2.1.1 Experimental Procedure

We used a gas-jet levitator at Department of Earth Science at Tohoku University (Fig. 1(a)), which was used in Nagashima et al. (2006) and modified for this study. An experimental chondrule was levitated on a gas diffuser and heated or cooled by adjusting the power of CO_2 laser. A series of experiments were conducted in a container filled with Ar gas or Ar(97%)-H_2(3%) mixture gas. Before the experiments, the air in the container was replaced for 15-30 minutes by Ar gas or Ar(97%)-H_2(3%) gas, and the same gas was used for the levitation. Iron metals appeared in the experimental chondrules, indicating a reduced condition was realized in the container. The oxygen fugacity in the container was calculated to be ΔIW-1.8 to ΔIW+1.9 from iron mole fraction in the silicate (pyroxene + mesostasis glass) and that in the metal in the experimental samples using the formula given in Corgne et al. (2008). The calculated oxygen fugacity indicates the redox condition at the retention temperature (Fig. 1(b)), the temperature just before the experimental chondrules were quenched. The oxygen fugacity has some ranges because the fugacity changes with the retention temperature. The redox conditions in our experiments match those in the chondrule formation regions where the oxygen fugacity ranged from approximately ΔIW-4 to ΔIW+1 (Villeneuve et al. 2015).

The approximate temperature curve during the experiments is shown in Fig. 1(b). First, a starting spherule was heated by a CO_2 laser at 1800 °C-2000 °C for 10 seconds, and we confirmed from the camera footage that the sample had melted completely. Afterward, the melted sample was cooled at about 60 °Cs^{-1} by adjusting the laser power and retained at a specific temperature below the liquidus (Table 1) for a few seconds to attain supercooling. At this temperature, we seeded the powder into the melted sample sphere. The seeds were the powder of the starting materials without sintering (mixtures of oxides of each element) or crushed crystals of experimental chondrules synthesized by the levitation system with the starting compositions. The oxide seed powders of the starting materials were 1-4 μm in diameter, and the crystal seed powders were adjusted to 42-52 μm by mesh sheets. The seed powder was sealed in a piston connected to a tube (Fig. 1(a)) and was introduced into the gas flow by

4

opening a clip. About 10-20 seeds collided with the melted sample surface in one experiment. The samples crystallized at the seeding temperature and, after crystallization, we retained the samples at a temperature close to the seeding temperature for a certain period of time (6-7200 sec.). The retention temperature is the average value during retention time and a little apart from the seeding temperature because the temperature was adjusted manually to keep it constant while the temperature fluctuates slightly due to sample vibration by the gas flow. The laser was then turned off, and the sample was quenched. In this experiment, we can choose the crystallization temperature (equal to the seeding temperature), the retention temperature (almost equal to the crystallization temperature), and the retention time as parameters (Table 2). The experimental chondrules produced by this procedure were polished to make thin sections or polished mounts and observed by electron microscopes. The analysis conditions are shown in 2.2.2.

2.1.2 Starting Material

We prepared four starting materials (Table 1): the mixtures of oxides of elements contained in RP chondrules. For iron, we used only FeO and no metallic iron was included in the starting material. RP-Fe1 and RP-Fe2, almost identical chemical compositions, were close to the average compositions of natural RP chondrules calculated from data of Dodd (1978), Lux et al. (1981), and Nagahara (1981). RP-lowFe is the bulk major-element composition of an RP chondrule in Y-790448 LL3.2 chondrite measured in this study, and this composition contains a smaller amount of iron than RP-Fe1 and RP-Fe2. RP-noFe is a normalized composition of average RP chondrules except iron and trace elements. The liquidus temperatures of these starting compositions were calculated by rhyolite-MELTS (v.1.0.x.) (Gualda et al. 2012), and those of RP-Fe1 and RP-Fe2 are 1574 °C. The liquidus temperatures of RP-lowFe and RP-noFe are 1569 °C and 1597 °C, respectively.

These starting materials were prepared as follows. First, the powder of starting material was

5

placed on a carbon plate set in the container filled with Ar-H_2 or Ar gas and sintered by the CO_2 laser. After that, the sintered material was floated on the diffuser by the gas flow and irradiated with the laser for about 10 seconds. The gases used in this step for each sample were the same that filled the container (Table 2). The materials melted and became a spherule due to surface tension. We used this sphere as a starting material. Subsequently, a series of levitation experiments were conducted. The spherule diameter ranges from 1.3-1.6 mm and the gas flow was 250-300 mlmin^{-1}. The list of experimental conditions and samples is shown in Table 2.

2.2. Natural Samples and Observation Procedures

2.2.1 Meteorite Samples

To compare with the experimentally produced chondrule samples, fourteen natural RP chondrules were chosen for the observation from chondrite meteorites that experienced the least degrees of aqueous alteration and thermal metamorphism because these secondary processes change the composition and mineralogy of chondrules: six chondrules from Y-82038 (H3.2) chondrite, seven from Y-790448 (LL3.2) chondrite, and one from Y-81020 (CO3.0) chondrite. These thin sections were provided by National Institute of Polar Research, Japan.

2.2.2 Observation and Analysis Procedure

The natural and experimental chondrules were observed and analyzed by field-emission scanning electron microscopy (FE-SEM/EDS: JEOL JSM-7001F) at Department of Earth Science at Tohoku University and field-emission electron probe microanalyzer (FE-EPMA/WDS: JEOL JXA 8530F) at Institute of Material Research at Tohoku University. The electron-beam acceleration voltage was 15 kV, the current was 1.0-1.4 nA for FE-SEM/EDS analysis, and 15 kV and 10 nA were used for FE-EPMA/WDS analysis.

3. Results

3.1 Crystallization Processes and Structures of Chondrules

The levitation experiments indicate that, when the seed particles collided with the melt sphere, pyroxene crystallization started from the contact points of the seeds (Fig. 2(a)). Low-Ca pyroxene was the only phase that crystallized. The crystal growth rates of the samples of RP-noFe composition, which were determined from the high-speed camera images, were very fast, about 0.2-1.3 mms^{-1}, and the whole sample crystallized within about 8 seconds. The sample temperature increased by about 50-100 °C for several seconds due to the recalescence caused by the latent heat release.

The chondrules produced by the experiments (Fig. 2(c), (f), (g)) were similar to the natural RP chondrules (Fig. 2(b), (d), (e)) in crystal morphologies. The pyroxenes were plates or fine dendritic shapes and grew radially from several points of seed contacts on the sample surface. The crystal textures were different between samples kept at a temperature of crystallization for shorter times (<160 s) and those retained for longer times (>500 s). In the samples with short retention times, Mg-rich pyroxene ("Mg-px" hereafter) crystallized (Fig. 2(f)). In contrast, relatively iron-rich pyroxene rims ("Fe-bearing px" hereafter) were observed on the surface of early-crystallized Mg-px in the samples with long retention times (Fig. 2(g)). Mesostasis glass was present in between pyroxene crystals. Iron metal inclusions appeared in the mesostasis glass in the long-retained samples.

On the other hand, the natural RP chondrules in meteorites also consisted of plate shape pyroxenes and mesostasis glass, and the mesostasis contained small inclusions of iron-nickel metals and iron sulfides (Fig. 2(d), (e)). In some natural chondrules, the elemental distribution in pyroxene crystals was almost homogeneous (Fig. 2(d)), while in other samples, the edges of pyroxene crystals (the brighter area in Fig. 2(e)) were enriched in iron compared with the inner part of pyroxene (the darker area in the same image), as were observed in pyroxene in the experimental RP chondrules (Fig. 2(g)) with long retention times. The dendritic pyroxene, as

observed in the experimental samples, was found in cryptocrystalline chondrules rather than typical RP chondrules.

3.2 Iron Partition Coefficient and Pyroxene Mg/(Mg+Fe) Ratios

Typical compositions of the natural RP chondrule and experimental RP chondrules are shown in Table 3. The analysis points by the electron microprobe were the center of mesostasis glass, the center of the pyroxene, and the zoned pyroxene rims. The pyroxene analysis parts (the center or rim) are shown in Supporting Data.

3.2.1 Natural Chondrules

The iron partition coefficient D_{Fe} is expressed as the ratio of iron mol% in pyroxene to that in mesostasis glass (D_{Fe} = Fe mol% $_{pyroxene}$/Fe mol%$_{mesostasis}$). The D_{Fe} of natural RP chondrules are plotted in Fig. 3(a), which shows variable D_{Fe} with an average of D_{Fe} = 2.7, higher than 1. This indicates that pyroxene is more enriched in iron than mesostasis glass in the natural RP chondrules.

Mg# of pyroxene (Mg# = Mg/(Mg+Fe) × 100) in natural RP chondrules are also plotted in Fig. 3(c), and the average Mg# is 77.0. Chondrules with Mg# > 90 are classified as Type I chondrules, and those with Mg# < 90 are Type II chondrules (McSween 1977; Scott & Taylor 1983). Observation showed that Type II RP chondrules are common in ordinary chondrites that we studied.

3.2.2 Experimental Samples

The experimental chondrules showed lower D_{Fe} than natural RP chondrules did (Fig. 3(b)). When the retention times after crystallization were less than 150 s, the average D_{Fe} was 0.4, indicating that the mesostasis was more iron-rich than pyroxene. The equilibrium D_{Fe} between

pyroxene and mesostasis glass was determined to be 0.37-0.65 in isothermal and slow cooling experiments of RP chondrules by Kennedy et al. (1993), whose starting compositions are relatively close to RP-Fe1 and RP-Fe2 in this study. D_{Fe} of short (<150 s) retained samples in this study were included within the range of equilibrium values. Whereas, when the retention times were longer than 1000 s, the average D_{Fe} was close to 1, and some exceeded 1. These high D_{Fe} were observed between Fe-bearing px (the rim formed on Mg-px) and mesostasis glass. In other words, samples that retained longer times have D_{Fe} closer to that of natural RP chondrules than those with short retention times.

The experimental samples showed higher Mg# than the natural RP chondrules did (Fig. 3(d)). The Mg# of Mg-px with short retention times (<160 s) were around 90 regardless of starting compositions. While with the long retention times (>500 s), Mg# of Fe-bearing px (the rim on Mg-px) were lowered and were close to that of natural RP chondrules (average Mg# of natural RP was 77.0). Mg# of Mg-px, inside Fe-bearing px (the center of pyroxene), were around 90, similar to Mg-px in the samples with short retention times. The outer parts of pyroxene in some of the natural RP chondrules were also enriched in iron than the inner part, like pyroxenes in the experimental samples (Fig. 2(e)). The gas kind (Ar-H_2 or Ar) used in experiments did not affect D_{Fe} and Mg# (Fig. 4(a), (b)). The plotted values in Fig. 4 are shown in Supporting Data.

4. Discussion

4.1 Constraints on the RP Chondrule Formation from Iron Partition Coefficients and Elemental Distribution

4.1.1 High Iron Partition Coefficients in Natural RP Chondrules

In the experimental samples of Kennedy et al. (1993) and experimental chondrules in this study with short retention times after crystallization (<150 s), D_{Fe} were as low as 0.3-0.7 (Fig.

9

3(b)). In contrast, natural RP chondrules show high D_{Fe} well above 1 ("Original" values in Fig. 3(a)) and the experimental chondrules that were retained for a long time after crystallization (>1000 s) showed D_{Fe} that close to or exceed 1 (Fig. 3(b)). The D_{Fe} difference is important because, in crystallization, whether D_{Fe} are less than or larger than 1 reflects more iron is distributed in the crystal or the mesostasis melt. Note that in this study, D_{Fe} of natural and experimental chondrules were defined as being established after the chondrule solidifications, not during crystallization.

The D_{Fe} similarity of natural chondrules and the experimental samples with long retention times indicates that both experienced the same process during formation. Thus, it constrains the formation process of natural RP chondrules.

First, we consider why D_{Fe} approached 1 in the experimental chondrules with increasing retention times. The first possible cause is the growth of Fe-bearing px. As Fe-bearing px grew, which contains more iron than underlying Mg-px, the iron content in the mesostasis glass decreased, because iron was supplied by mesostasis glass, not by Mg-px. As a result, D_{Fe} increased and approached 1 (D_{Fe} were defined between Fe-bearing px and mesostasis).

The second cause is the reduction of FeO to metallic iron in the mesostasis melt due to the long retention times in a reduced atmosphere (Fig. 2(g)). In most cases, the samples with long retention times had the metals in mesostasis glass. The occurrences of the iron metal inclusions in the experimental chondrules are similar to iron-nickel metals or sulfides observed in natural RP chondrules (Fig. 2(d) and (e)). Mesostasis glass near the metal boundary is darker in the BSE image (Fig. 2(g)). It means that iron is more depleted than the average mesotasis glass, suggesting that the metals nucleated in the mesostasis melt after the pyroxene growth. Since the valence of iron in the starting material was only divalent (FeO), the divalent iron in the mesostasis was reduced and metals were formed before the solidification of mesostasis melt into the glass. When the metals crystallized in the mesostasis melt, the reduced iron in the mesostasis was absorbed by (concentrated into) the metal crystals and thus iron content in the mesositasis was reduced. As a result, D_{Fe} between pyroxene and mesostasis glass increased.

A similar process can be considered for natural RP chondrules. iron-nickel metals and sulfides were commonly distributed in the mesostasis glass of natural RP chondrules (Fig. 2(d), (e)). After the pyroxene growth, FeO in the mesostasis melt might have been reduced or sulfurized, and the iron metals or iron sulfides nucleated in the melt. As a result, FeO content in the mesostasis decreased, and the high D_{Fe} were established in natural RP chondrules. In fact, "Corrected D_{Fe}", which we re-calculated D_{Fe} between pyroxene and whole mesostasis (total iron concentration in mesostasis glass including metal and sulfide inclusions), are plotted around 1 (Fig. 3(a)). Therefore, D_{Fe} in natural RP chondrules should be "apparent D_{Fe}" that was established after pyroxene growth and does not represent iron distribution during crystal growth. D_{Fe} in the experimental chondrules containing iron metals are lower compared to natural RP chondrules (Fig. 3(a)and (b)), possibly because longer retention times or more reduced gas in the protoplanetary disk facilitated the formation of iron metal inclusions, which resulted in the increase in D_{Fe}.

4.1.2 Pyroxene Composition in Natural and Experimental RP Chondrules

Natural RP chondrules, at least in ordinary chondrites we studied, were commonly classified as Type II based on their pyroxene compositions. In the experiments with short retention times (<160 s), Mg-px (Fig. 2(f)) crystallized and showed higher Mg# (average was about 90) compared with that in natural chondrules. In contrast, Fe-bearing px (Fig. 2(g)) crystallized with long retention times (>500 s) had Mg# close to that in natural RP chondrules. The long retention times after crystallization simulates slow cooling after crystallization. Thus, the natural RP chondrules might have been cooled slowly after the crystallization enough to grow Fe-bearing px.

In the experimental chondrules with long retention times, the occurrence of Fe-bearing px is considered to be the result of the overgrowth on earlier-formed Mg-px or the iron diffusion from mesostasis to the rim of Mg-px. In particular, textures of the overgrowth are remarkable:

the sharp boundaries between Mg-px and Fe-bearing px, and structures where more than two pyroxene plates fuse by Fe-bearing px (Fig. 2(g)). The overgrowth and or iron diffusion can explain the low pyroxene Mg# in natural RP chondrules.

We investigated the possibility that the oxygen fugacity during crystallization may change the ion valence and affect the pyroxene Mg#. Our experiments suggest that there were no relationships between pyroxene Mg# and the oxygen fugacity controlled by gas species (Ar-H2 or Ar) (Fig. 4 (c)). In addition, the crystallization temperature also did not affect pyroxene Mg# (Fig. 4 (d)). The plotted values in Fig. 4 are shown in Supporting Data.

Therefore, it is suggested that natural RP chondrules were produced by pyroxene crystallization followed by cooling slow enough to allow the crystallization of metal and sulfide inclusions in the mesostasis melt, diffusion of iron from mesostasis into pyroxene, and overgrowth of Fe-bearing px on earlier formed Mg-px. Experimental further studies about the reduction and the sulfidation of mesostasis, the effects of the cooling rates of chondrules, and the ambient gas conditions would constrain the chondrule formation events.

4.2 Crystallization of RP Chondrules by Seeding

The high-speed camera images (Fig. 2(a)) showed that the radial pyroxene crystallized by heterogeneous nucleation from the seed contact points. In the protoplanetary disk, the interplanetary dust could collide with chondrule melts as the seeds. The collisions are possible due to the high dust densities in the chondrule-forming regions (Ebel & Grossman 2000; Fedkin & Grossman 2013). If we suppose that RP chondrules crystallized by collisions with dust grains, the number density of dust grains that existed during chondrule formation events can be estimated. For instance, the mass density of chondrule itself and the chondrule mass density in chondrule-forming regions are assumed to be $3.0 \, \mathrm{gcm^{-3}}$(Ciesla et al. 2004) and $6 \times 10^{-12} \, \mathrm{gcm^{-3}}$(Arakawa & Nakamoto 2019), respectively, and the chondrule diameter is set to 0.5 mm. The chondrule number density of $3.8 \times 10^{-9} \, \mathrm{cm^{-3}}$ is given from these values, and

the number density of the dust grains is assumed to be higher than that of chondrules because not all dust collide with chondrules.

5. Conclusion

Heating experiments of RP chondrules in a reduced atmosphere with natural RP chondrule compositions reproduced the radial texture of low-Ca pyroxene crystals and interstices mesotasis glass. Comparison between experimentally-reproduced chondrules and natural chondrules indicate that the high iron partition coefficients between pyroxene and mesostasis glass in natural RP chondrules are explained by the process of iron removal from the mesostasis due to the formation of the metal inclusions in the mesostasis melt. The growth of iron-rich secondary pyroxene partly explains the variation of the Mg# of pyroxene in natural RP chondrules during the slow cooling. Natural RP chondrules experienced slow cooling that allowed these processes to occur.

References

Arakawa, S., & Nakamoto, T. 2019, ApJ, 877, 84

Bollard, J., Connelly, J. N., & Bizzarro, M. 2015, M&PS, 50, 1197

Ciesla, F. J., & Hood, L. L. 2002, Icar, 158, 281

Ciesla, F. J., Lauretta, D. S., & Hood, L. L. 2004, M&PS, 39, 531

Connolly, H. C., & Hewins, R. H. 1995, GeCoA, 59, 3231

Connolly, H. C., Jones, B. D., & Hewins, R. H. 1998a, GeCoA, 62, 2725

Connolly Jr, H. C., & Love, S. G. 1998b, Sci, 280, 62.

Corgne, A., Keshav, S., Wood, B. J., McDonough, W. F., & Fei, Y. 2008, GeCoA, 72, 574

Desch, S. J., & Cuzzi, J. N. 2000, Icar, 143, 87

Dodd, R. T. 1978, E&PS, 40, 71

Ebel, D. S., & Grossman, L. 2000, GeCoA, 64, 339

Fedkin, A. V, & Grossman, L. 2013, GeCoA, 112, 226

Grossman, L., Beckett, J. R., Fedkin, A. V., Simon, S. B., & Ciesla, F. J. 2008, RvMG, 70, 371

Gualda, G. A., Ghiorso, M. S., Lemons, R. V., & Carley, T. L. 2012, JPet, 53, 875.

Johansen, A., & Okuzumi, S. 2018, A&AC, 609, A31.

Johnson, B. C., Bowling, T. J., & Melosh, H. J. 2014, Icar, 238, 13

Johnson, B. C., Minton, D. A., Melosh, H. J., & Zuber, M. T. 2015, Natur, 517, 339

Kennedy, A. K., Lofgren, G. E., & Wasserburg, G. J. 1993, E&PSL, 115, 177

Kieffer, S. W. 1975, Sci, 189, 333.

Kita, N. T., & Ushikubo, T. 2012, M&PS, 47, 1108

Hewins, R. H. 1983, Chondrules and their Origins, 122(1st ed.; Lunar and Planetary Institute)

Hewins, R. H., & Radomsky, P. M. 1990, Metic, 25, 309

Lofgren, G. 1989, GeCoA, 53, 461

Lofgren, G., & Lanier, A. B. 1990, GeCoA, 54, 3537

Lofgren, G., & Russell, W. J. 1986, GeCoA, 50, 1715

Lux, G., Keil, K., & Taylor, G. J. 1981, GeCoA, 45, 675

Mcsween, H. Y. 1977, GeCoA, 41, 1843

Mishra, B., Manvar, P., Choudhury, K., & Karagadde, S. 2020, NatSR, 10, 1

Morris, M. A., & Desch, S. J. 2010, ApJ, 722, 1474.

Nagahara, H. 1981, Memoirs of National Institute of Polar Research. Special issue, 20, 145

Nagashima, K., Moriuchi, Y., Tsukamoto, K., Tanaka, K. K., & Kobatake, H. 2008, JMPeS, 103, 204

Nagashima, K., Tsukamoto, K., Satoh, H., Kobatake, H., & Dold, P. 2006, JCrGr, 293, 193

Pack, A., Kremer, K., Albrecht, N., Simon, K., & Kronz, A. 2010, Geochem. Trans., 11, 1

Pape, J., Mezger, K., Bouvier, A. S., & Baumgartner, L. P. 2019, GeCoA, 244, 416

Scott, E. R. D., & Taylor, G. J. 1983, JGR, 88 Suppl, 275

Shete, G., Mishra, S., Karagadde, S., & Srivastava, A. 2021, NatSR, 11, 1

Tsuchiyama, A., & Nagahara, H. 1981, Memoirs of National Institute of Polar Research.

Special issue,

20, 175

Tsuchiyama, A., Nagahara, H., & Kushiro, I. 1980, E&PSL, 48, 15

Tsukamoto, K., Satoh, H., Takamura, Y., & Kuribayashi, K. 1999, in 24th Symp. Antarctic

Meteorites

(Tokyo: NIPR), 24, 179

Villeneuve, J., Libourel, G., & Soulié, C. 2015, GeCoA, 160, 277

Wakita, S., Matsumoto, Y., Oshino, S., & Hasegawa, Y. 2017, ApJ, 834, 125

Whipple, F. L. 1966. Sci, 153, 54

Table 1 Starting material compositions in weight %

	RP-Fe1	RP-Fe2	RP-lowFe	RP-noFe
Na_2O	1.0	0.8	1.2	1.1
MgO	26.5	26.4	26.0	30.2
Al_2O_3	2.5	2.3	2.6	3.0
SiO_2	56.1	55.0	58.9	64.0
CaO	1.6	2.0	1.6	1.9
FeO	12.2	13.6	9.8	0.0
Total	99.9	100.1	100.1	100.2
Liquidus(°C)	1574.0	1574.0	1569.0	1597.0
Emissivity	0.65	0.65	0.66	0.80

Table 2 Samples and experimental conditions

Run#	Starting material	Gas	Seed	Crystallized temperature (°C)	Retention temperature (°C)	Retention time(s)
0710-1	RP-lowFe	Ar	oxide powder	1063	1063	15
0710-3	RP-lowFe	Ar	oxide powder	1063	1063	57
0728-2	RP-lowFe	Ar-H$_2$	crystal powder	1043	1052	100
0728-3	RP-lowFe	Ar-H$_2$	crystal powder	1057	1050	100
0728-4	RP-lowFe	Ar-H$_2$	crystal powder	1059	1066	100
0728-10	RP-lowFe	Ar-H$_2$	crystal powder	1040	1037	100
0728-14	RP-lowFe	Ar-H$_2$	crystal powder	1146	1138	100
0902-1	RP-lowFe	Ar-H$_2$	oxide powder	1241	1252	148
0902-4	RP-lowFe	Ar-H$_2$	oxide powder	1469	1477	21
0902-8	RP-lowFe	Ar-H$_2$	oxide powder	1552	1537	39
0902-10	RP-lowFe	Ar-H$_2$	oxide powder	1270	1257	15
0919-1	RP-Fe1	Ar-H$_2$	crystal powder	1480	1294	20
0919-2	RP-Fe1	Ar-H$_2$	crystal powder	1532	1411	21
0919-7	RP-Fe1	Ar-H$_2$	crystal powder	1479	1483	48
0919-9	RP-Fe1	Ar-H$_2$	crystal powder	1498	1536	3600
0919-11	RP-Fe1	Ar-H$_2$	crystal powder	1480	1494	2400
1111-1	RP-Fe1	Ar	crystal powder	1422	1422	6
1111-4	RP-Fe1	Ar	crystal powder	1313	1313	24
1111-6	RP-Fe1	Ar	crystal powder	1274	1274	10
1111-7	RP-Fe1	Ar	crystal powder	1267	1267	10
1128-1	RP-Fe1	Ar-H$_2$	no seeding	not determined	1549	4680
1128-2	RP-Fe1	Ar-H$_2$	no seeding	not determined	1545	6000
1128-3	RP-Fe1	Ar-H$_2$	no seeding	not determined	1505	2074
1128-6	RP-Fe1	Ar-H$_2$	no seeding	not determined	1533	960
1128-7	RP-Fe1	Ar-H$_2$	no seeding	not determined	1536	7200
1208-2	RP-Fe2	Ar-H$_2$	no seeding	not determined	1430	523
1208-4	RP-Fe2	Ar-H$_2$	no seeding	not determined	1396	1800
1208-5	RP-Fe2	Ar-H$_2$	no seeding	1460	1420	7200
0204-4	RP-noFe	Air	crystal powder	1404	1404	12
0403-7	RP-noFe	Air	crystal powder	1395	1395	9
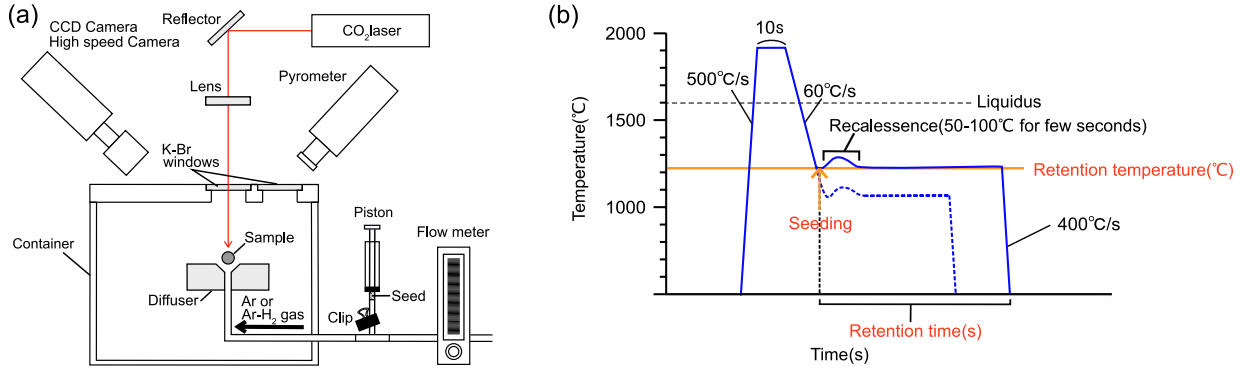
Fig. 1 Overview of the experimental instrument and temperature profile.

(a) Gas-jet levitator under the reduced condition. A CO_2 laser (LC-100NV from DEOS) irradiated a levitated experimental sample, and the laser power was adjusted for heating and cooling. A reflector set the path of the laser beam, and a lens adjusted the beam to cover the entire sample. The sample was placed on a diffuser and floated by the gas flow ejected through a tube connected to the diffuser. A flow meter controlled the gas flow rate. In-situ observations were conducted by a CCD camera (Elmo) and a high-speed monochrome camera (Photron FASTCAM-Net Max). The temperature was measured with a pyrometer (LUMASENSE TECHNOLOGIES ImpacIN140/5-H). The pyrometer measured 5.14 μm wavelength in 500-2500 °C, and the minimum measurement spot was 1.3 mm in diameter. The experiments were conducted in a container to control the redox state. A lid of the container had a valve opened during the experiments to allow gas to displace the inside air. K-Br windows on the lid transmitted the laser beam and emission from the sample for temperature measurements by the pyrometer. (b)Temperature profile during experiments. A solid blue line is an example, and the crystalized temperature, retention temperature, and retention time were changed as parameters like a dashed line. The operation detail is shown in 2.1.1.
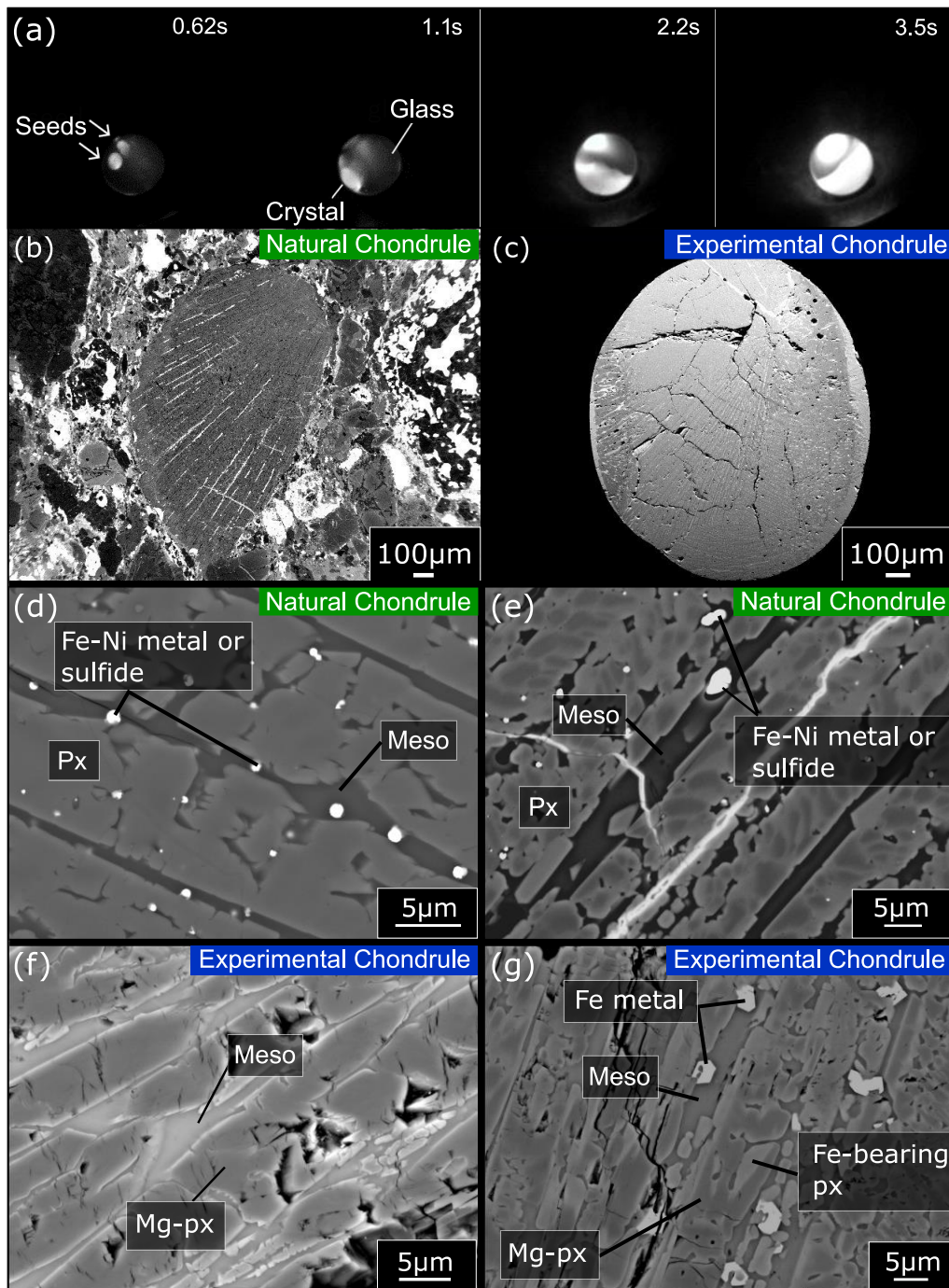
Fig. 2 In-situ observation and the textures of the natural and experimental RP chondrules. (a)Images of the high-speed camera during in-situ observation. Brighter areas are crystals. The upper right values represent the time from the moment that the seeds were attached to the sample surface. The laser irradiated from above the sample, and the sample rotated during levitation. (b)-(g) Backscattered electron (BSE) images of the natural and experimental chondrules, (b) RP chondrule in Y-790448(LL3.2), 57-2, thin section, (c) Run#1208-2 experimental chondrule, (d) RP chondrule in Y-790448(LL3.2), 57-1, thin section, and (e) RP chondrule in Y-790448(LL3.2), 57-2, thin section, (f) Run#0919-1 experimental chondrule, and (g) Run#0919-11 experimental chondrule. Meso = mesostasis glass.

19
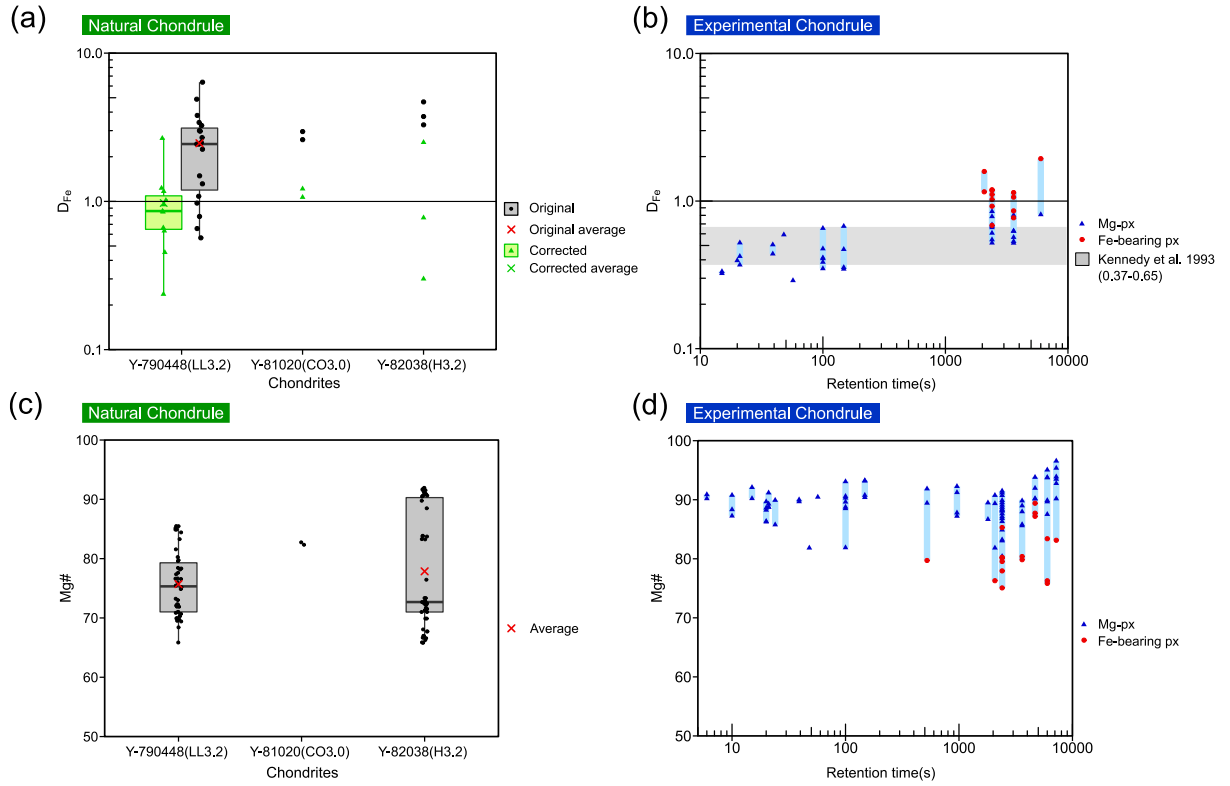
Fig. 3 Comparison of the natural and experimental chondrules. (a) Boxplot of D_{Fe} of natural chondrules with interquartile range and whiskers from the minimum to the maximum value. "Original" is the analyzed value. "Corrected" is the D_{Fe} derived from iron in pyroxene and that in whole mesostasis (mesostasis glass including metals and sulfides). (b) D_{Fe} in experimental chondrules. Mg# in (c) natural chondrules (boxplot) and (d)experimental. Blue lines in (b) and (d) represent the minimum to max values range. In (b) and (d), Mg-px and Fe-bearing px regions overlap in some places. Because we define them in a single crystal, the Mg-px in some crystals are iron-rich relative to Fe-bearing px in other crystals.
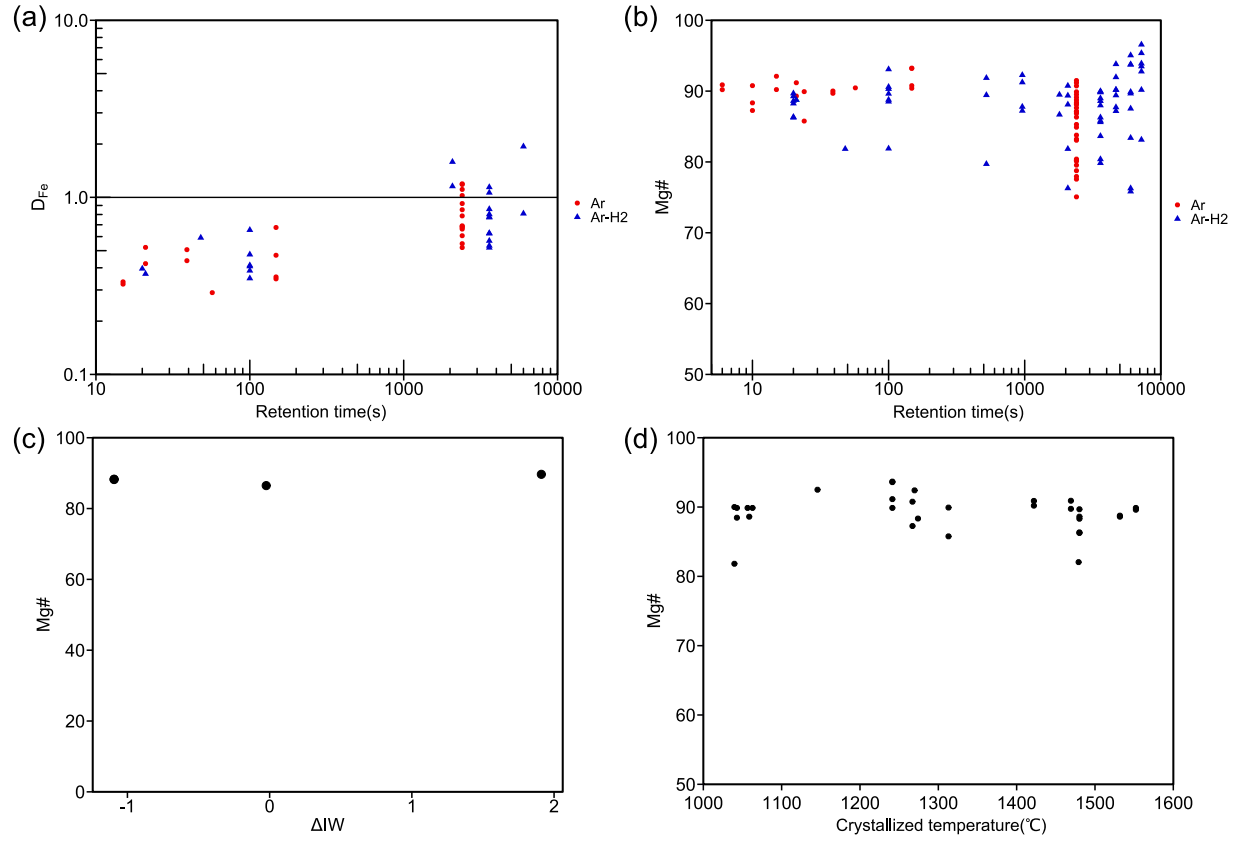
Fig. 4 Relationships between gas used in experiments and (a)D_{Fe}, (b)pyroxene Mg#, and relationships Mg# and (c) oxygen fugacity, (d)crystallized temperature.

Supporting Data

Plotted data in Fig. 3.

(a)DFe (Natural chondrules)

Chondrite name	DFe	Original/Corrected	Analysis part*
Y-790448(LL3.2)	6.37	Original	core
Y-790448(LL3.2)	3.25	Original	core
Y-790448(LL3.2)	2.69	Original	core
Y-790448(LL3.2)	4.89	Original	core
Y-790448(LL3.2)	2.49	Original	core
Y-790448(LL3.2)	2.98	Original	core
Y-790448(LL3.2)	3.49	Original	rim
Y-790448(LL3.2)	2.25	Original	core
Y-790448(LL3.2)	2.43	Original	rim
Y-790448(LL3.2)	2.44	Original	rim
Y-790448(LL3.2)	1.08	Original	core
Y-790448(LL3.2)	3.41	Original	core
Y-790448(LL3.2)	4.14	Original	rim
Y-790448(LL3.2)	0.57	Original	rim
Y-790448(LL3.2)	0.66	Original	core
Y-790448(LL3.2)	1.31	Original	core
Y-790448(LL3.2)	0.79	Original	core
Y-790448(LL3.2)	1.49	Original	core
Y-790448(LL3.2)	0.97	Original	core
Y-790448(LL3.2)	2.67	Corrected	core
Y-790448(LL3.2)	1.02	Corrected	rim
Y-790448(LL3.2)	0.63	Corrected	core
Y-790448(LL3.2)	0.86	Corrected	core
Y-790448(LL3.2)	1.23	Corrected	core
Y-790448(LL3.2)	0.95	Corrected	core
Y-790448(LL3.2)	1.17	Corrected	core
Y-790448(LL3.2)	0.85	Corrected	core
Y-790448(LL3.2)	0.24	Corrected	core
Y-790448(LL3.2)	0.66	Corrected	core
Y-790448(LL3.2)	0.45	Corrected	rim
Y-81020(CO3.0)	2.96	Original	core
Y-81020(CO3.0)	2.61	Original	core
Y-81020(CO3.0)	1.22	Corrected	core
Y-81020(CO3.0)	1.07	Corrected	core

Y-82038(H3.2)	3.28	Original	rim
Y-82038(H3.2)	3.74	Original	rim
Y-82038(H3.2)	4.69	Original	rim
Y-82038(H3.2)	2.5	Corrected	rim
Y-82038(H3.2)	0.3	Corrected	rim
Y-82038(H3.2)	0.78	Corrected	rim

*Notes: core = DFe between the center of pyroxene and the center of mesostasis glass, rim = DFe between iron-rich zoned rim in pyroxene and the center of mesostasis glass

(b)DFe (Experimental chondrules)

Run#	Retention time(s)	DFe	Analysis part*
0710-1	15	0.32	core
0710-3	57	0.29	core
0728-2	100	0.41	core
0728-2	100	0.41	core
0728-3	100	0.39	core
0728-4	100	0.48	core
0728-10	100	0.65	core
0728-10	100	0.35	core
0902-1	148	0.36	core
0902-1	148	0.35	core
0902-1	148	0.68	core
0902-1	148	0.47	core
0902-4	21	0.52	core
0902-4	21	0.42	core
0902-8	39	0.51	core
0902-8	39	0.44	core
0902-10	15	0.33	core
0919-1	20	0.4	core
0919-2	21	0.37	core
0919-7	48	0.59	core
0919-9	3600	1.14	core
0919-9	3600	0.8	core
0919-9	3600	0.63	core
0919-9	3600	0.78	core
0919-9	3600	0.53	core
0919-9	3600	1.06	rim
0919-9	3600	0.86	core
0919-9	3600	0.63	core
0919-9	3600	0.77	core
0919-9	3600	0.52	core
0919-9	3600	0.57	core
0919-11	2400	0.52	core
0919-11	2400	1.02	rim
0919-11	2400	0.69	core
0919-11	2400	1.18	rim
0919-11	2400	0.79	core

0919-11	2400	0.85	core
0919-11	2400	0.61	core
0919-11	2400	0.55	core
0919-11	2400	0.68	rim
0919-11	2400	0.92	core
0919-11	2400	1.11	rim
0919-11	2400	0.66	core
0919-11	2400	1.19	core
0919-11	2400	0.67	core
1128-2	6000	0.81	core
1128-2	6000	1.94	core
1128-3	2074	1.59	core
1128-3	2074	1.16	core

*Notes: core = DFe between the center part of pyroxene (Mg-px) and the center of mesostasis glass, rim = DFe between iron-rich rim (Fe-bearing px) and the center of mesostasis glass

(c)Mg# (Natural chondrules)

Chondrite name	Mg#	Analysis part*
Y-790448(LL3.2)	85.16	core
Y-790448(LL3.2)	84.42	core
Y-790448(LL3.2)	85.47	core
Y-790448(LL3.2)	85.49	core
Y-790448(LL3.2)	83.29	core
Y-790448(LL3.2)	84.9	core
Y-790448(LL3.2)	84.9	core
Y-790448(LL3.2)	70.28	core
Y-790448(LL3.2)	77.62	core
Y-790448(LL3.2)	80.26	core
Y-790448(LL3.2)	78.34	core
Y-790448(LL3.2)	74.87	core
Y-790448(LL3.2)	72.3	core
Y-790448(LL3.2)	73.24	core
Y-790448(LL3.2)	73.02	core
Y-790448(LL3.2)	71.03	core
Y-790448(LL3.2)	71.89	core
Y-790448(LL3.2)	71.01	core
Y-790448(LL3.2)	72.08	core
Y-790448(LL3.2)	65.86	core
Y-790448(LL3.2)	69.73	core
Y-790448(LL3.2)	69.41	core
Y-790448(LL3.2)	76.57	core
Y-790448(LL3.2)	78.44	core
Y-790448(LL3.2)	69.53	core
Y-790448(LL3.2)	69.93	core
Y-790448(LL3.2)	76.03	core
Y-790448(LL3.2)	75.45	core
Y-790448(LL3.2)	79.74	core
Y-790448(LL3.2)	69.97	core
Y-790448(LL3.2)	68.41	core
Y-790448(LL3.2)	72.27	core
Y-790448(LL3.2)	81.57	core
Y-790448(LL3.2)	78.17	core
Y-790448(LL3.2)	70.86	core
Y-790448(LL3.2)	79.58	core
Y-790448(LL3.2)	77.36	rim

Y-790448(LL3.2)	76.62	core
Y-790448(LL3.2)	76.66	core
Y-790448(LL3.2)	70.69	rim
Y-790448(LL3.2)	71.9	core
Y-790448(LL3.2)	75.2	core
Y-81020(CO3.0)	82.34	core
Y-81020(CO3.0)	82.75	core
Y-82038(H3.2)	91.19	core
Y-82038(H3.2)	90.47	core
Y-82038(H3.2)	91.66	core
Y-82038(H3.2)	91.53	core
Y-82038(H3.2)	90.86	core
Y-82038(H3.2)	90.64	core
Y-82038(H3.2)	91.94	core
Y-82038(H3.2)	65.8	core
Y-82038(H3.2)	66.67	core
Y-82038(H3.2)	68.06	core
Y-82038(H3.2)	66.28	core
Y-82038(H3.2)	66.58	core
Y-82038(H3.2)	65.88	core
Y-82038(H3.2)	67.72	core
Y-82038(H3.2)	71.3	core
Y-82038(H3.2)	69.9	core
Y-82038(H3.2)	71	core
Y-82038(H3.2)	72.68	core
Y-82038(H3.2)	72.48	core
Y-82038(H3.2)	73.35	core
Y-82038(H3.2)	66.98	core
Y-82038(H3.2)	72.32	core
Y-82038(H3.2)	76.45	core
Y-82038(H3.2)	71.5	core
Y-82038(H3.2)	83.29	core
Y-82038(H3.2)	83.79	core
Y-82038(H3.2)	83.25	core
Y-82038(H3.2)	83.73	core
Y-82038(H3.2)	83.85	core
Y-82038(H3.2)	72.48	core
Y-82038(H3.2)	73.35	core
Y-82038(H3.2)	66.98	core

Y-82038(H3.2)	72.32	core
Y-82038(H3.2)	67.72	core
Y-82038(H3.2)	71.3	core
Y-82038(H3.2)	69.9	core
Y-82038(H3.2)	71	core
Y-82038(H3.2)	72.68	core
Y-82038(H3.2)	72.93	core
Y-82038(H3.2)	72.17	core
Y-82038(H3.2)	71.52	core
Y-82038(H3.2)	71.69	core
Y-82038(H3.2)	88.49	core
Y-82038(H3.2)	89.76	core
Y-82038(H3.2)	91.73	core
Y-82038(H3.2)	90.59	core
Y-82038(H3.2)	91.37	core
Y-82038(H3.2)	90.91	core
Y-82038(H3.2)	91.05	core
Y-82038(H3.2)	91.89	core

*Notes: core = the center of pyroxene, rim = iron-rich zoned rim in pyroxene

(d)Mg# (Experimental chondrules)

Run#	Retention time(s)	Mg#	Analysis part
0710-1	15	90.22	Mg-px
0710-3	57	90.46	Mg-px
0728-2	100	89.63	Mg-px
0728-2	100	88.52	Mg-px
0728-3	100	90.31	Mg-px
0728-4	100	88.78	Mg-px
0728-10	100	81.89	Mg-px
0728-10	100	90.59	Mg-px
0728-14	100	93.08	Mg-px
0902-1	148	93.2	Mg-px
0902-1	148	93.25	Mg-px
0902-1	148	90.4	Mg-px
0902-1	148	90.77	Mg-px
0902-4	21	89.3	Mg-px
0902-4	21	91.18	Mg-px
0902-8	39	90.01	Mg-px
0902-8	39	89.69	Mg-px
0902-10	15	92.1	Mg-px
0919-1	20	88.26	Mg-px
0919-1	20	86.35	Mg-px
0919-1	20	88.62	Mg-px
0919-1	20	89.68	Mg-px
0919-1	20	86.26	Mg-px
0919-2	21	88.76	Mg-px
0919-2	21	88.76	Mg-px
0919-7	48	81.84	Mg-px
0919-9	3600	80.38	Fe-bearing px
0919-9	3600	85.81	Mg-px
0919-9	3600	88.99	Mg-px
0919-9	3600	85.62	Mg-px
0919-9	3600	79.84	Fe-bearing px
0919-9	3600	87.99	Mg-px
0919-9	3600	89.83	Mg-px
0919-11	2400	80.13	Fe-bearing px
0919-11	2400	88.21	Mg-px
0919-11	2400	75.07	Fe-bearing px
0919-11	2400	79.54	Fe-bearing px

0919-11	2400	88.75	Mg-px
0919-11	2400	88.41	Mg-px
0919-11	2400	89.9	Mg-px
0919-11	2400	91.5	Mg-px
0919-11	2400	91.18	Mg-px
0919-11	2400	77.95	Fe-bearing px
0919-11	2400	90.74	Mg-px
0919-11	2400	89.11	Mg-px
0919-11	2400	87.15	Mg-px
0919-11	2400	84.9	Mg-px
0919-11	2400	83.06	Mg-px
0919-11	2400	86.84	Mg-px
0919-11	2400	88.1	Mg-px
0919-11	2400	85.29	Fe-bearing px
0919-11	2400	80.25	Fe-bearing px
0919-11	2400	89.52	Mg-px
0919-11	2400	86.32	Mg-px
0919-11	2400	83.22	Mg-px
0919-11	2400	87.64	Mg-px
0919-11	2400	80.41	Mg-px
1111-1	6	90.89	Mg-px
1111-1	6	90.2	Mg-px
1111-4	24	89.92	Mg-px
1111-4	24	85.77	Mg-px
1111-6	10	88.34	Mg-px
1111-7	10	90.77	Mg-px
1111-7	10	87.26	Mg-px
1128-1	4680	93.81	Mg-px
1128-1	4680	89.41	Fe-bearing px
1128-1	4680	87.72	Fe-bearing px
1128-1	4680	91.96	Mg-px
1128-1	4680	90.19	Mg-px
1128-1	4680	90.17	Mg-px
1128-1	4680	87.19	Fe-bearing px
1128-2	6000	93.77	Mg-px
1128-2	6000	87.53	Mg-px
1128-2	6000	93.75	Mg-px
1128-2	6000	95.06	Mg-px
1128-2	6000	83.4	Fe-bearing px

1128-2	6000	89.89	Mg-px
1128-2	6000	75.83	Fe-bearing px
1128-2	6000	89.67	Mg-px
1128-2	6000	76.28	Fe-bearing px
1128-3	2074	89.37	Mg-px
1128-3	2074	90.76	Mg-px
1128-3	2074	76.29	Fe-bearing px
1128-3	2074	81.84	Mg-px
1128-6	960	92.27	Mg-px
1128-6	960	87.23	Mg-px
1128-6	960	87.79	Mg-px
1128-6	960	91.24	Mg-px
1128-7	7200	93.49	Mg-px
1128-7	7200	96.57	Mg-px
1128-7	7200	93.89	Mg-px
1128-7	7200	95.36	Mg-px
1128-7	7200	92.78	Mg-px
1128-7	7200	90.18	Mg-px
1208-2	523	89.44	Mg-px
1208-2	523	79.71	Fe-bearing px
1208-2	523	91.86	Mg-px
1208-4	1800	86.68	Mg-px
1208-4	1800	89.49	Mg-px
1208-5	7200	91.54	Fe-bearing px
1208-5	7200	83.14	Fe-bearing px

Plotted data in Fig. 4.

   The starting composition of 1226-3, 1226-6, and 1226-8 was RP-Fe2 with 1 wt% NiO added. The addition of NiO was to confirm that the oxygen fugacity in the container was below the NiNiO(nickel-nickel oxide) buffer.

(a)DFe and gas

Run#	Gas	Retention time(s)	DFe
0710-1	Ar	15	0.32
0710-3	Ar	57	0.29
0728-2	Ar-H2	100	0.41
0728-2	Ar-H2	100	0.41
0728-3	Ar-H2	100	0.39
0728-4	Ar-H2	100	0.48
0728-10	Ar-H2	100	0.65
0728-10	Ar-H2	100	0.35
0902-1	Ar	148	0.36
0902-1	Ar	148	0.35
0902-1	Ar	148	0.68
0902-1	Ar	148	0.47
0902-4	Ar	21	0.52
0902-4	Ar	21	0.42
0902-8	Ar	39	0.51
0902-8	Ar	39	0.44
0902-10	Ar	15	0.33
0919-1	Ar-H2	20	0.4
0919-2	Ar-H2	21	0.37
0919-7	Ar-H2	48	0.59
0919-9	Ar-H2	3600	0.53
0919-9	Ar-H2	3600	0.86
0919-9	Ar-H2	3600	0.77
0919-9	Ar-H2	3600	0.57
0919-9	Ar-H2	3600	0.78
0919-9	Ar-H2	3600	1.06
0919-9	Ar-H2	3600	0.63
0919-9	Ar-H2	3600	0.52
0919-9	Ar-H2	3600	1.14
0919-9	Ar-H2	3600	0.8
0919-9	Ar-H2	3600	0.63
0919-11	Ar	2400	0.52
0919-11	Ar	2400	1.18
0919-11	Ar	2400	0.85

0919-11	Ar	2400	1.02
0919-11	Ar	2400	0.69
0919-11	Ar	2400	0.79
0919-11	Ar	2400	0.61
0919-11	Ar	2400	0.55
0919-11	Ar	2400	0.68
0919-11	Ar	2400	0.92
0919-11	Ar	2400	1.11
0919-11	Ar	2400	0.66
0919-11	Ar	2400	1.19
0919-11	Ar	2400	0.67
1128-2	Ar-H2	6000	0.81
1128-2	Ar-H2	6000	1.94
1128-3	Ar-H2	2074	1.59
1128-3	Ar-H2	2074	1.16

(b)Mg# and gas

Run#	Gas	Retention time(s)	Mg#	Analysis part
0710-1	Ar	15	90.22	Mg-px
0710-3	Ar	57	90.46	Mg-px
0728-2	Ar-H2	100	89.63	Mg-px
0728-2	Ar-H2	100	88.52	Mg-px
0728-3	Ar-H2	100	90.31	Mg-px
0728-4	Ar-H2	100	88.78	Mg-px
0728-10	Ar-H2	100	81.89	Mg-px
0728-10	Ar-H2	100	90.59	Mg-px
0728-14	Ar-H2	100	93.08	Mg-px
0902-1	Ar	148	93.2	Mg-px
0902-1	Ar	148	93.25	Mg-px
0902-1	Ar	148	90.4	Mg-px
0902-1	Ar	148	90.77	Mg-px
0902-4	Ar	21	89.3	Mg-px
0902-4	Ar	21	91.18	Mg-px
0902-8	Ar	39	90.01	Mg-px
0902-8	Ar	39	89.69	Mg-px
0902-10	Ar	15	92.1	Mg-px
0919-1	Ar-H2	20	88.26	Mg-px
0919-1	Ar-H2	20	86.35	Mg-px
0919-1	Ar-H2	20	88.62	Mg-px
0919-1	Ar-H2	20	89.68	Mg-px
0919-1	Ar-H2	20	86.26	Mg-px
0919-2	Ar-H2	21	88.76	Mg-px
0919-2	Ar-H2	21	88.76	Mg-px
0919-7	Ar-H2	48	81.84	Mg-px
0919-9	Ar-H2	3600	85.62	Mg-px
0919-9	Ar-H2	3600	79.84	Fe-bearing px
0919-9	Ar-H2	3600	87.99	Mg-px
0919-9	Ar-H2	3600	89.83	Mg-px
0919-9	Ar-H2	3600	80.38	Fe-bearing px
0919-9	Ar-H2	3600	85.81	Mg-px
0919-9	Ar-H2	3600	88.99	Mg-px
0919-11	Ar	2400	77.95	Fe-bearing px
0919-11	Ar	2400	84.9	Mg-px
0919-11	Ar	2400	83.06	Mg-px

0919-11	Ar	2400	86.84	Mg-px
0919-11	Ar	2400	88.1	Mg-px
0919-11	Ar	2400	85.29	Fe-bearing px
0919-11	Ar	2400	80.25	Fe-bearing px
0919-11	Ar	2400	80.13	Fe-bearing px
0919-11	Ar	2400	88.21	Mg-px
0919-11	Ar	2400	79.54	Fe-bearing px
0919-11	Ar	2400	88.41	Mg-px
0919-11	Ar	2400	89.52	Mg-px
0919-11	Ar	2400	75.07	Fe-bearing px
0919-11	Ar	2400	88.75	Mg-px
0919-11	Ar	2400	89.9	Mg-px
0919-11	Ar	2400	86.32	Mg-px
0919-11	Ar	2400	83.22	Mg-px
0919-11	Ar	2400	87.64	Mg-px
0919-11	Ar	2400	80.41	Mg-px
0919-11	Ar	2400	89.11	Mg-px
0919-11	Ar	2400	87.15	Mg-px
0919-11	Ar	2400	91.5	Mg-px
0919-11	Ar	2400	91.18	Mg-px
0919-11	Ar	2400	90.74	Mg-px
1111-1	Ar	6	90.89	Mg-px
1111-1	Ar	6	90.2	Mg-px
1111-4	Ar	24	85.77	Mg-px
1111-4	Ar	24	89.92	Mg-px
1111-6	Ar	10	88.34	Mg-px
1111-7	Ar	10	90.77	Mg-px
1111-7	Ar	10	87.26	Mg-px
1128-1	Ar-H2	4680	93.81	Mg-px
1128-1	Ar-H2	4680	89.41	Fe-bearing px
1128-1	Ar-H2	4680	87.72	Fe-bearing px
1128-1	Ar-H2	4680	91.96	Mg-px
1128-1	Ar-H2	4680	90.19	Mg-px
1128-1	Ar-H2	4680	90.17	Mg-px
1128-1	Ar-H2	4680	87.19	Fe-bearing px
1128-2	Ar-H2	6000	93.77	Mg-px
1128-2	Ar-H2	6000	87.53	Mg-px
1128-2	Ar-H2	6000	93.75	Mg-px
1128-2	Ar-H2	6000	95.06	Mg-px

1128-2	Ar-H2	6000	83.4	Fe-bearing px
1128-2	Ar-H2	6000	89.89	Mg-px
1128-2	Ar-H2	6000	75.83	Fe-bearing px
1128-2	Ar-H2	6000	89.67	Mg-px
1128-2	Ar-H2	6000	76.28	Fe-bearing px
1128-3	Ar-H2	2074	89.37	Mg-px
1128-3	Ar-H2	2074	90.76	Mg-px
1128-3	Ar-H2	2074	76.29	Fe-bearing px
1128-3	Ar-H2	2074	81.84	Mg-px
1128-6	Ar-H2	960	92.27	Mg-px
1128-6	Ar-H2	960	87.23	Mg-px
1128-6	Ar-H2	960	87.79	Mg-px
1128-6	Ar-H2	960	91.24	Mg-px
1128-7	Ar-H2	7200	93.49	Mg-px
1128-7	Ar-H2	7200	96.57	Mg-px
1128-7	Ar-H2	7200	93.89	Mg-px
1128-7	Ar-H2	7200	95.36	Mg-px
1128-7	Ar-H2	7200	92.78	Mg-px
1128-7	Ar-H2	7200	90.18	Mg-px
1208-2	Ar-H2	523	89.44	Mg-px
1208-2	Ar-H2	523	79.71	Fe-bearing px
1208-2	Ar-H2	523	91.86	Mg-px
1208-4	Ar-H2	1800	86.68	Mg-px
1208-4	Ar-H2	1800	89.49	Mg-px
1208-5	Ar-H2	7200	91.54	Fe-bearing px
1208-5	Ar-H2	7200	83.14	Fe-bearing px

(c)DFe and ΔIW

Run#	ΔIW	DFe	Starting material	Gas	Seed	Crystallized temperature (°C)	Retention temperature (°C)	Retention time(s)
1226-3	-0.02	0.33	RP-Fe2	Ar	crystal powder	1290	1290	22
1226-6	1.91	0.25	RP-Fe2	Ar-H2	crystal powder	1286	1461	14
1226-8	-1.09	0.39	RP-Fe2	Ar-H2	crystal powder	1268	1344	34

(d)Mg# and crystallized temperature

Run#	Crystallized temperature (°C)	Mg#	Analysis part
0710-3	1063	89.87	Mg-px
0728-2	1043	89.87	Mg-px
0728-2	1043	88.46	Mg-px
0728-3	1057	89.87	Mg-px
0728-4	1059	88.61	Mg-px
0728-10	1040	81.82	Mg-px
0728-10	1040	90.59	Mg-px
0728-14	1146	93.08	Mg-px
0902-1	1241	93.67	Mg-px
0902-1	1241	93.59	Mg-px
0902-1	1241	89.87	Mg-px

0902-1	1241	91.14	Mg-px
0902-4	1469	89.74	Mg-px
0902-4	1469	90.91	Mg-px
0902-8	1552	89.87	Mg-px
0902-8	1552	89.61	Mg-px
0902-10	1270	92.41	Mg-px
0919-1	1480	88.31	Mg-px
0919-1	1480	86.35	Mg-px
0919-1	1480	88.62	Mg-px
0919-1	1480	89.68	Mg-px
0919-1	1480	86.26	Mg-px
0919-2	1532	88.61	Mg-px
0919-2	1532	88.76	Mg-px
0919-7	1479	82.05	Mg-px
1111-1	1422	90.89	Mg-px
1111-1	1422	90.2	Mg-px
1111-4	1313	85.77	Mg-px
1111-4	1313	89.92	Mg-px
1111-6	1274	88.34	Mg-px
1111-7	1267	90.77	Mg-px
1111-7	1267	87.26	Mg-px